Alleviating Orbital-Angular-Momentum-Mode Dispersion Using a Reflective Metasurface

Shan Jiang,[1,2] Chang Chen,[1,2,*] Jun Ding,[3] Hualiang Zhang,[4] and Weidong Chen[1,2]

[1] *Department of Electronic Engineering and Information Science, University of Science and Technology of China, Hefei 230027, China*

[2] *Key Laboratory of Electromagnetic Space Information, Chinese Academy of Sciences, Hefei 230027, China*

[3] *School of Physics and Electronic Science, East China Normal University, Shanghai, 200241, China*

[4] *Department of Electrical and Computer Engineering, University of Massachusetts Lowell, Lowell 01854, USA*

(Received 15 January 2020; revised manuscript received 20 March 2020; accepted 15 April 2020; published 15 May 2020)

Electromagnetic waves carrying orbital angular momentum (OAM) have attracted much interest due to their capacity to enhance communication capabilities. In this work, the OAM-mode-dispersion (OMD) phenomenon is analyzed by decomposing the vortex wave into a series of plane waves based on the spectral-domain method. Specifically, the OMD phenomenon induced by off-axis transmission is analyzed in detail, which clearly demonstrates that the vortex wave with a single OAM mode is spread to multiple OAM modes after off-axis propagation. To avoid the performance degradation of the OAM system due to OMD (e.g., interchannel crosstalk and signal-to-noise ratio reduction), a method for alleviating the OMD based on the reflective metasurface is proposed to transmit or receive the vortex waves with multiple OAM modes. Theoretical formulas for the phase distribution are developed in order to construct the metasurface. As proof-of-concept demonstrations, two metasurface prototypes are designed, fabricated, and measured to verify the proposed method in the radio-frequency range. The experimental results agree very well with the full-wave simulation results, validating the design methodology.

DOI: 10.1103/PhysRevApplied.13.054037

I. INTRODUCTION

Electromagnetic waves can carry not only energy but also orbital angular momentum (OAM) due to wave-particle duality. This physical property of the electromagnetic field has been widely studied and utilized in the optical regime due to the particle properties of the photon at short wavelengths [1–3]. Meanwhile, it is an intriguing question whether this property can find applications in the microwave domain to serve radar or communication systems. To answer this question, three fundamental issues need to be addressed. First, how can we generate a vortex wave efficiently in the low-frequency radio domain? A uniform circular array (UCA) phased by $e^{il\varphi}$ is a simple way that has been proposed in 2007 [4] to radiate vortex radio waves. Since then, many methods have been reported to generate OAM waves, including spiral-phase-plate metasurfaces [5,6], defect structures [7,8], higher-mode radiation [9–11], and so on, leading to compact [12], broadband [13], and multiplexing designs [14–16]. Second, how can we receive and demultiplex OAMs at the receiving end? In general, there are two common receiving schemes, namely whole-aperture-sampling receiving (WASR) and partial-aperture-sampling receiving (PASR) [17]. Third, we need to identify the means of modeling the radio-vortex-wave propagation properties and predicting the link budget. The transmission characteristics of a radio vortex wave have been initially investigated in 2015 [18]. Recently, a generalized Friis transmission equation for radio OAMs has been proposed [19], which represents great progress in this research area. Also, OAM reflection, refraction, and interaction with certain complicated targets have been studied in Ref. [20,21]. Although there are still controversies on whether there are distinct differences between OAM-based radio technology and multiple-input–multiple-output (MIMO) technology [22,23], a large number of applications have verified the OAM-based systems' capabilities for achieving super-resolution radar imaging and detection [24–32] and improving the channel capacity [33–38].

Although the works mentioned above have demonstrated the widespread applications of OAM-based systems, ranging from wireless communication to radar, most of the existing works assume the line-of-sight (LOS) model, which is a simplification of the realistic situation. In the real world, during the propagation of the OAM waves, reflection, refraction, diffraction, and even atmospheric turbulence could occur [33], which would inevitably distort

*chench@ustc.edu.cn

the wave front of the original OAM waves and lead to the dispersion of the topological charges. In this work, this phenomenon is defined as OAM-mode dispersion (OMD). The OMD breaks the orthogonality among different OAM channels, resulting in interchannel crosstalk and a signal-to-noise ratio reduction, which could greatly degrade the performance of OAM-based systems. Therefore, the aim of this work is to theoretically demonstrate the OMD phenomenon and design a reflective anti-OMD metasurface to alleviate this issue. The main contributions of this work are twofold: (1) this work attempts to study the OMD phenomenon quantitatively and systematically by using the spectral-domain method (SDM); and (2) a systematic OMD alleviation methodology based on the reflective metasurface is proposed. The proposed method has great potential to be applied in super-resolution imaging or communication systems that suffer from OMD. The paper is organized as follows: in Sec. II, the OMD is analyzed and demonstrated by SDM in detail; in Sec. III, the OMD alleviation method based on the reflective metasurface is proposed and validated through full-wave simulations and experiments; and brief conclusions are drawn in Sec. IV.

II. PROPAGATION ANALYSIS OF OAM WAVES

Several issues that occur in radar and wireless communication systems (e.g., off-axis transmission, multipath propagation, and partial-aperture-sampling receiving) are likely to deteriorate the purity of the OAM spectrum, which usually leads to system-performance degradation. To quantitatively understand the impact of these issues on an OAM system, we analyze the OMD phenomenon based on the SDM. One typical scenario (i.e., off-axis transmission) as shown in Fig. 1 is studied in detail in this work. In Fig. 1, both the transmitter (Tx) and the receiver (Rx) are reflective metasurfaces and the displacement between Tx and Rx is denoted as D. The radii of Tx and Rx are denoted as R_t and R_r, respectively.

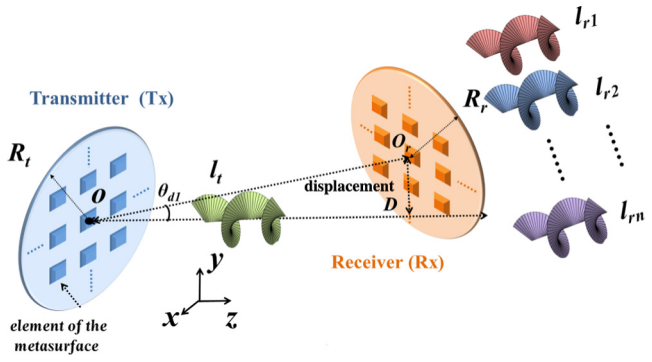

FIG. 1. A schematic view of an off-axis orbital-angular-momentum (OAM) transmission system. Both the transmitter and the receiver are metasurfaces composed of $M \times N$ elements to radiate and detect the OAM waves.

Before analyzing the OMD phenomenon, the mathematical model for far-field radiation of an OAM system based on an ultrathin circular metasurface is built up by Fourier transformation. The aperture field of the metasurface can be written as

$$\vec{\mathbf{E}} = E(\rho')\, e^{-jl\varphi'}\hat{y}, \tag{1}$$

where $E(\rho')$ is the amplitude-distribution function of the electric field along the radial direction under the y-polarized incidence, l is the topological charge, and (r,θ,φ) is the spherical coordinate. In this work, the $e^{-j\omega t}$ time convention is assumed. According to the Fourier relation between the aperture field and the radiation field, the radiation field can be expressed by

$$\vec{\mathbf{E}}_{\text{rad}}(\mathbf{r}) = C_1 \frac{e^{jkr}}{4\pi r}\int_0^R E(\rho')\rho'\, d\rho' \int_0^{2\pi} \times e^{-jl\varphi'} e^{jk\rho' \sin\theta\cos(\varphi'-\varphi)}\, d\varphi'\hat{y}, \tag{2}$$

where k is the magnitude of wave vector in the propagation medium, R is the radius of the metasurface, and $C_1 = jk(1+\cos\theta)$. The observation and source points are denoted by (r,θ,φ) and $(\rho',\varphi',0)$ in spherical and cylindrical coordinates, respectively. By using variable substitution and the integral relationship of the lth Bessel function, the general radiation-field expression in Eq. (2) can be simplified as

$$\vec{\mathbf{E}}_{\text{rad}}(\mathbf{r}) = 2\pi j^n C_1 \frac{e^{jkr}}{4\pi r} e^{-jl\varphi}\int_0^R E(\rho')\rho' J_l\left(k\rho'\sin\theta\right) d\rho'\hat{y} \tag{3}$$

where J_l is the lth-order Bessel function of the first kind. Here, we assume that $E(\rho')$ is constant and we ignore the effect of C_1. Detailed derivations from Eq. (1) to Eq. (3) can be found in Appendix A.

According to the classic electromagnetic theory, arbitrary waves (including OAM waves) can be decomposed into plane waves by the SDM [17]. Then, the radiation field carrying OAM waves expressed by Eq. (3) can be expanded into the superposition of infinite plane waves, as

$$F(x,y,z) = \frac{j}{4\pi^2}\iint_{k_x^2+k_y^2<k^2} \Psi(k_x,k_y) e^{j(k_x x+k_y y+k_z z)}\, dk_x\, dk_y, \tag{4}$$

where

$$\Psi(k_x,k_y) = e^{-jl\varphi}\int_0^R \rho' J_l\left(k\rho'\sin\theta\right) d\rho' = \int_0^R\int_0^{2\pi} \frac{\rho'}{k_z} e^{jk_\rho\rho'\cos(\zeta-\varphi)} e^{-jl\zeta}\, d\zeta\, d\rho', \tag{5}$$

$$k_x^2 + k_y^2 + k_z^2 = k^2, \quad k_\rho = k\sin(\theta), \\ k_x = k_\rho\cos(\varphi), \quad k_y = k_\rho\sin(\varphi). \tag{6}$$

Detailed derivations from Eq. (4) to Eq. (6) can be found in Appendix B. The complex amplitude of each plane wave is determined by $\Psi\left(k_x, k_y\right)$ and the propagation direction depends on the wave vector $\left(k_x, k_y, k_z\right)$. In this way, the propagation analysis of OAM waves can be transformed into the analysis of a series of plane waves, which is simpler and more comprehensible. The amplitude and phase distributions of the series of plane waves for two OAM systems with $l = 2$ and 4 are illustrated in Fig. 2, with $R =$ 50 mm at 6 GHz. It can be observed from Figs. 2(a) and 2(c) that the dominant amplitude components of the plane waves concentrate on a narrow annular domain, which indicates that the wave vectors of these plane waves form a cone rotating around the z axis and most of the energy is reserved in this annular region. Moreover, it can be noted that the outer radius of the annular ring (focal ring) becomes larger when the topological charge increases. The calculated phase pattern for $l = 2$ ($l = 4$) as shown in Fig. 2(b) [Fig. 2(d)] clearly demonstrates the phase changes of 4π (8π) around a circle. Based on these properties, we propose a method for radiating multiple OAM modes by constructing different OAM modes in different annular rings of the metasurface. In addition, Fig. 3 plots the cone angle ($\theta_{\max}$) with respect to different topological charges for different radii of the metasurface. It can be observed from Fig. 3 that the cone angle (θ_{max}) increases as the topological charge increases and the radius of the metasurface decreases, indicating that a larger aperture is required to recover an OAM wave carrying higher-order modes.

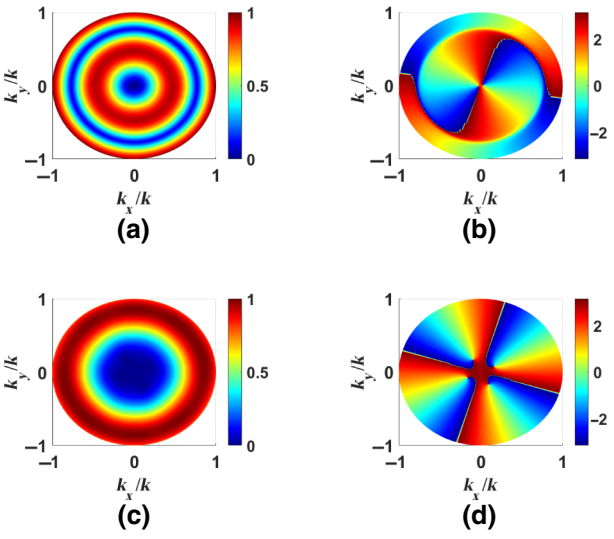

FIG. 2. The visual representation of $\Psi\left(k_x, k_y\right)$: the amplitude distribution, (a) $l = 2$ and (c) $l = 4$, and the phase distribution, (b) $l = 2$ and (d) $l = 4$. The operation frequency is 6 GHz and the radius of the metasurface, R, is 50 mm.

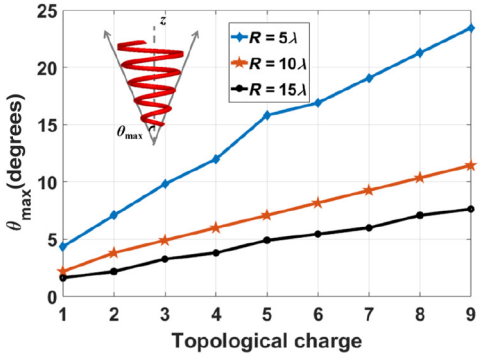

FIG. 3. The propagation directions of the maximum plane-wave components vary with the radii and topological charges.

Therefore, arbitrary OAM waves radiated by the metasurface can be considered as the superposition of a series of plane waves and the propagation characteristics of each plane wave is known. In the following, the off-axis transmission is discussed and we show how the SDM can be used in the OMD analysis.

To show the mechanism of the mode-dispersion phenomenon clearly, the phase and magnitude distributions on the receiver aperture are calculated by MATLAB and the full-wave simulator (HFSS v. 19). In the HFSS simulation, the parameters are configured as follows: the receiving plane is a circle with a radius of one wavelength, the distance between Tx and Rx is five wavelengths, and the operation frequency is set to be 6 GHz. The transmitter Tx or excitation source used here is a single circular metasurface with a radius of one wavelength. The OAM-purity calculation is based on the complex Fourier transform. Since the azimuthal angle φ is a periodic function, its Fourier conjugate, the OAM, is a discrete variable and the corresponding Fourier relationship is given in Ref. [39] by

$$A_l = \frac{1}{2\pi}\int_0^{2\pi} \psi(\varphi)\, d\varphi\, e^{-jl\varphi}, \tag{7}$$

$$\psi(\varphi) = \sum_l A_l e^{jl\varphi}. \tag{8}$$

Only topological charges ranging from -10 to 10 are considered in the following sections, because the higher-order ($> |6|$) topological charges are trivial enough to be neglected in the scenarios ($l = -2, D \leq 0.6\lambda$) under investigation.

Considering an OAM off-axis transmission link as shown in Fig. 1, a Tx transmits an l_lth-OAM wave and an l_2th-OAM receiver (Rx) is utilized to receive the signal. Usually, in the on-axis situation, the signal can be recovered only when $l_1 = l_2$, due to the orthogonality of the OAM waves. However, in the off-axis situation, the normalized amplitude of the received wave can be written as

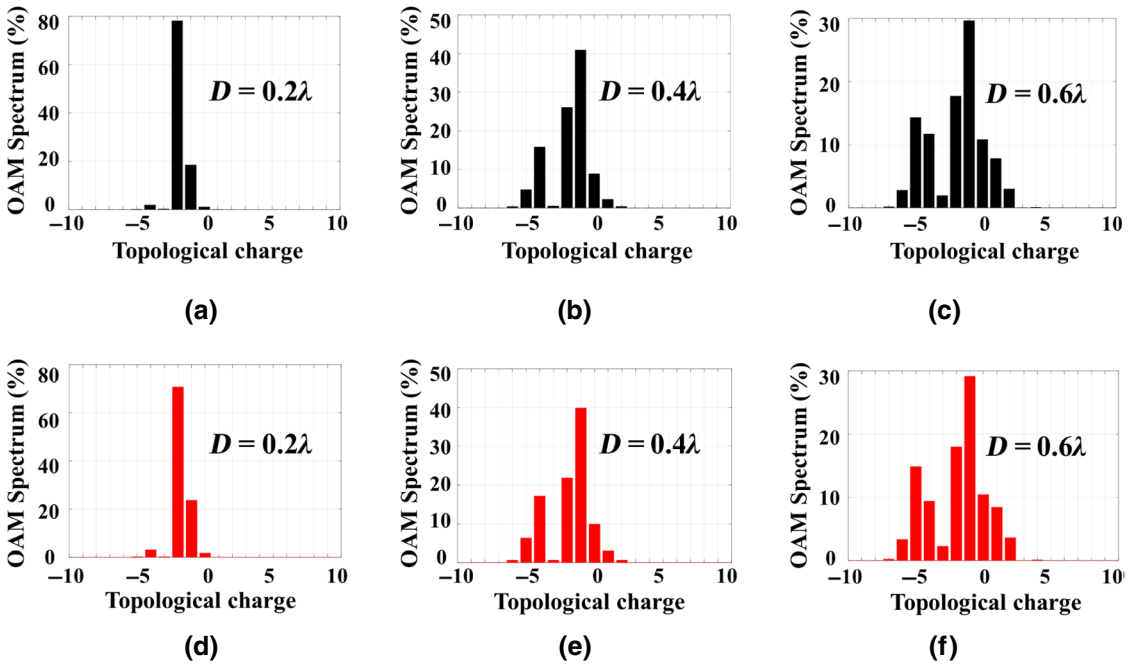

FIG. 4. The OAM purities in off-axis transmission with a dominant transmission OAM mode of $l = -2$ by varying the displacement between Tx and Rx: (a)–(c) results calculated by MATLAB; (d)–(f) results simulated by HFSS. (a),(d) $D = 0.2\lambda$; (b),(e) $D = 0.4\lambda$; (c),(f) $D = 0.6\lambda$.

$F(x_r, y_r, z_r)$ as follows:

$$F(x,y,z) = \frac{j}{4\pi^2} \iint_{k_x^2+k_y^2<k^2} \Psi\left(k_x, k_y\right) \times e^{j\left(k_x x + k_y (y+D) + k_z z\right)} \, dk_x \, dk_y, \tag{9}$$

where D is the displacement between Rx and Tx.

The OAM purities of the received signal with a dominant mode of $l = -2$ in off-axis transmission with different displacements are shown in Fig. 4, where Figs. 4(a)–4(c) and Figs. 4(d)–4(f) are the results calculated by MATLAB and those simulated by HFSS, respectively. It can be seen from Fig. 4 that these two sets of results agree very well with each other. Moreover, it can be noted that the received wave spreads to more OAM modes when the displacement increases, indicating a worse OMD phenomenon. Furthermore, for other scenarios, such as multipath transmission and multiple-object scattering, similar phenomena can be observed and the OMD will affect the system performance.

III. OMD-ALLEVIATION METHOD BASED ON REFLECTIVE METASURFACE

As discussed in the previous section, the OMD usually cannot be avoided during OAM transmission in the real world. Therefore, to improve the OAM system performance, it is highly desirable to harvest as many OAM modes as we can in the dispersed OAM spectrum. In this work, a method is proposed to address this issue based on the reflective metasurface as illustrated in Fig. 5(a), which can generate or receive multiple OAM modes in pairs $(\pm l_l, \pm l_2, \ldots, \pm l_N)$. The method is based on the observations presented in previous sections that the directions of the main lobes vary with the topological charges and radii of the metasurfaces. Thus, in the proposed method, the whole metasurface is divided into N regions for $2N$ OAM modes, as shown in Fig. 5(b), and each region corresponds to superimposed OAM modes of $\pm l_i$ $(i = 1, \ldots, N)$. The N regions are composed of a circular region with a radius of R_l and $N-1$ annual rings. The inner and outer radii of the nth annual ring are denoted as R_{n-1} and R_n, respectively. The circular area is for the OAM mode with the minimum number of l_1 and each annual ring corresponds to the assigned OAM modes.

A. Derivation of the method

If only two-mode OAM (i.e., $\pm l_1$) is considered, the metasurface consists of only the central area. The two-mode metasurface composed of $M \times M$ metal-patch elements is illuminated by a feeding horn antenna located at the position of vector $\mathbf{r}_f$, as shown in Fig. 5(a). To harvest two OAM modes of $\pm l_1$, the required phase shift at each element for generating two OAM modes can be derived as

$$\phi_{mn} = -\arg[\cos(l_1\varphi_{mn}) + \cos(-l_1\varphi_{mn})] - k_0\left|\mathbf{r_{mn}} - \mathbf{r_f}\right|, \tag{10}$$

where $\mathbf{r}_{mn}$ is the position vector of the mnth element and k_0 is the wave vector in vacuum.

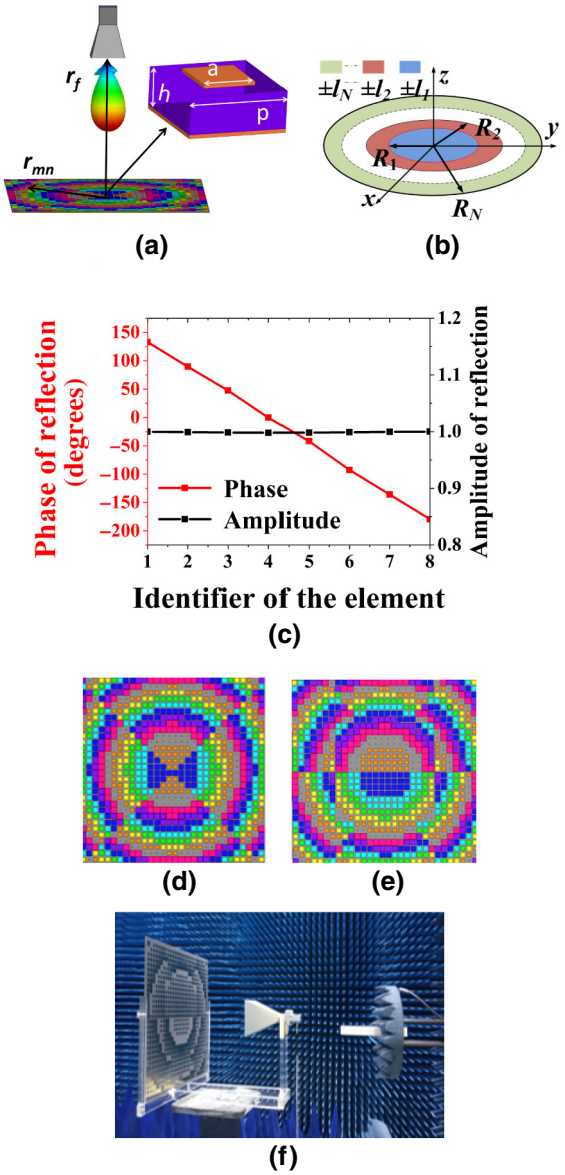

FIG. 5. (a) The configuration of the two-mode OAM metasurface and the structure of the metasurface element. (b) The configuration of the metasurface for generating multiple OAM modes. (c) The amplitudes and phases of reflections for the eight elements simulated at 6 GHz. (d) A top view of the metasurface for two complementary multiple OAM modes ($l = \pm 2$). (e) A top view of the metasurface for four multiple OAM modes ($l = \pm 1, l = \pm 3$). (f) The experimental system configuration for measuring the vortex wave front using the near-field scanning technique.

According to the phase distribution given in Eq. (10), the radiation electric field of the reflective metasurface can be calculated by the superposition principle:

$$E(\theta,\varphi) = \cos\theta \sum_{m=1}^{M}\sum_{n=1}^{M} C_{mn} e^{jk_0|\mathbf{r_{mn}}-\mathbf{r_f}|}(e^{jl_1\varphi_{mn}} + e^{-jl_1\varphi_{mn}}), \tag{11}$$

where C_{mn} is the pattern function of the mnth element. Therefore, according to Eq. (11), two-mode OAM ($\pm l_l$) with almost the same electric field intensity can be obtained.

To generate more OAM modes, it is necessary to divide the whole metasurface into N regions, each of which corresponds to the superimposed modes of $\pm l_i$ ($i = 1, \ldots, N$). Considering that $|J_l(\cdot)| = |J_{-l}(\cdot)|$, the following equations need to be satisfied (assuming that the designed angle of the main-lobe direction of the vortex waves is θ_M) and the phase-shift distribution in each region between R_{i-1} and R_i satisfies Eq. (10) for different l_i:

$$\left|\int_0^{R_1} J_{l_1}(k\rho' \sin\theta_M)\, d\rho'\right| = \left|\int_{R_1}^{R_2} J_{l_2}(k\rho' \sin\theta_M)\, d\rho'\right| \cdots = \left|\int_{R_{N-1}}^{R_N} J_{l_N}(k\rho' \sin\theta_M)\, d\rho'\right|. \tag{12}$$

Thus, to design a reflective metasurface with four modes of $\pm l_1 = 1$ and $\pm l_2 = 3$, R_1 and R_2 are calculated to be $8p$ and $30p$, respectively, according to Eq. (12), where p is periodicity of the metasurface element.

B. Simulated and measured results

To realize the required phase distribution of the metasurface, metal-patch structures are utilized, as depicted in the inset of Fig. 5(a). By using the frequency-domain solver in HFSS, we plot the amplitude and phase distributions of eight selected metasurface elements at 6 GHz in Fig. 5(c). These eight metasurface elements are labeled as 1, 2, 3, 4, 5, 6, 7, and 8, with corresponding lengths of 1.0, 9.3, 10.4, 11.1, 11.6, 12.3, 13.4, and 15.0 (in millimeters), respectively. It can be seen from Fig. 5(c) that a reflective 2π phase coverage with a phase step of $\pi/4$ can be achieved and that the reflective amplitudes are kept almost the same (close to unity). As proof-of-concept demonstrations, we design two reflective metasurfaces with superimposed two-OAM modes ($\pm l_l = 2$) and four-OAM modes ($\pm l_1 = 1$ and $\pm l_2 = 3$). The required phase delays ϕ_{mn} for the mnth element are calculated using Eqs. (10) and (12) Accordingly, the phase distributions of the two-mode OAM ($\pm l_l = 2$) and four-mode OAM ($\pm l_l = 1$ and $\pm l_2 = 3$) waves are depicted in Figs. 5(d) and 5(e), respectively. In order to show the phase distributions clearly, in Figs. 5(d) and 5(e) we use different-colored patches to represent different phases. Moreover, the phase distributions of more metasurfaces with other multiple superimposed OAM modes are illustrated in Fig. 8 (see Appendix C).

Considering the reflective metasurfaces composed of 30×30 elements, the operating frequency and the periodicity of the metasurface element are set to be 6 GHz

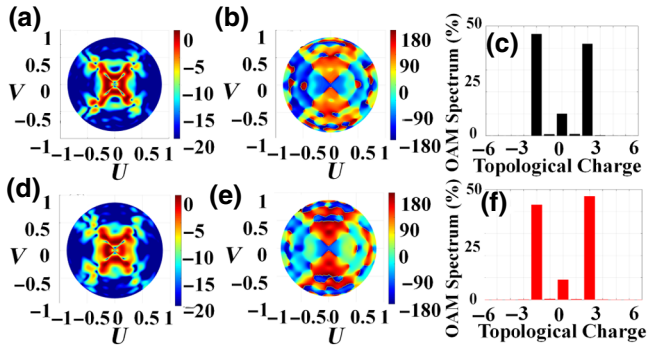

FIG. 6. The two-mode OAM metasurface for generating $\pm l_l = 2$. Simulated results: (a) the amplitude pattern; (b) the phase pattern; (c) the OAM-mode purities. Measured results: (d) the amplitude pattern; (e) the phase pattern; (f) the OAM-mode purities.

and $p = 15$ mm, respectively. These two designed metasurfaces are simulated by the full-wave simulator HFSS, fabricated by printed-circuit-board (PCB) technology and characterized by a near-field scanning system in an anechoic chamber. The measurement setups are shown in Fig. 5(f). The position vector of the feeding source r_f is set to be $(0, 0, 0.75 \times 30 \times 15$ mm). Figures 6 and 7 depict the simulated and measured results for the two-mode OAM and four-mode OAM, respectively. Figures 6(a) and 6(b) and Figs. 6(d) and 6(e) plot the simulated (measured) amplitude and phase of the normalized three-dimensional radiation pattern in the u-v plane ($u = \sin\theta\cos\varphi$, $v = \sin\theta\cos\varphi$) for the two-mode OAM, respectively, while Fig. 6(c) [Fig. 6(f)] shows the OAM spectra calculated by Eqs. (7) and (8). It can be observed that the simulated results and measured results agree very well with each other, which validates the design methodology. Besides, it can be noted that the energy null caused by the phase

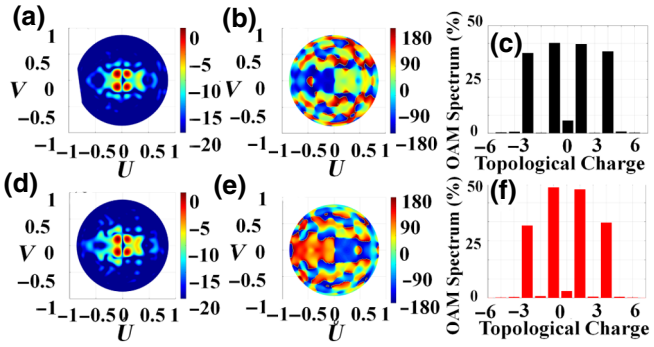

FIG. 7. The four-mode OAM metasurface for generating $\pm l_1 = 1$ and $\pm l_2 = 3$. Simulated results: (a) the amplitude pattern; (b) the phase pattern; (c) the OAM-mode purities. Measured results: (d) the amplitude pattern; (e) the phase pattern; (f) the OAM-mode purities.

singularity is clearly observed in Figs. 6(a) and 6(d). The phase distributions shown in Figs. 6(b) and 6(e) are different from the single-mode OAM phase distribution. Furthermore, it can be seen from Fig. 6(f) that the dominant modes for the two-mode OAM wave are -2 and $+2$ as desired. The measured mode purities for modes -2 and $+2$ are 43% and 46%, respectively and hence are approximately equal. Some phase noise occurs at other modes, which might be due to the quantization loss. Similar conclusions can be drawn from Fig. 7 for the four-mode OAM case. It is worth mentioning that the purities of the different OAM modes are designed to be approximately equal in this method, as expressed in Eqs. (11) and (12), which could be of great interest for the application of super-resolution imaging. Furthermore, the purities of the different radiated OAM modes can be designed to achieve arbitrary ratios.

IV. CONCLUSION

To summarize, the OMD phenomenon is theoretically analyzed by SDM and a method for alleviating the OMD is proposed using reflective metasurfaces. In general, although the receiver can fully recover the information from an OAM transmitter with the same mode in ideal on-axis transmission, the OMD phenomenon usually emerges during real-world transmission and affects the system performance. The OMD phenomenon caused by off-axis transmission is analyzed in detail, which clearly demonstrates that the single-mode OAM beam is spread into multiple OAM modes. Besides, according to the spectral-domain decomposition method, it is observed that the energy of the vortex beam is concentrated in an annular ring for a certain OAM mode in the spectral domain and that the inner radius of the ring increases as the topological charge increases. Based on this property, a method based on reflective metasurfaces is developed to alleviate the OMD, in which the whole metasurface is divided into N regions and each region corresponds to two OAM modes of $\pm$l. Correspondingly, two metasurface prototypes are designed, fabricated, and measured to verify the theoretical analysis and full-wave simulations at 6 GHz. The experimental results agree very well with the simulation results, validating the design methodology. The proposed method could pave the way toward the application of OAM waves in microwave radar imaging and wireless communication systems with a much-reduced mode-dispersion effect.

ACKNOWLEDGMENTS

We would like to thank Information Science Laboratory Center of USTC for the measurement services. This work was supported by the Natural Science Foundation of China under Grant No. 61971392.

APPENDIX A

The lth Bessel function has the following integral relationship: [40]

$$J_l(z) = \frac{j^{-n}}{2\pi}\int_0^{2\pi} e^{j(z\cos\varphi - l\varphi)}\,d\varphi. \tag{A1}$$

Then, using the variable substitution $t = \varphi' - \varphi$, the general radiation field can be simplified as

$$\begin{aligned}\overrightarrow{\mathbf{E}}_{\text{rad}}(\mathbf{r}) &= C_1\frac{e^{jkr}}{4\pi r}\int_0^R E(\rho')\rho'\,d\rho'\int_0^{2\pi} e^{-jl(t+\varphi)}e^{jk\rho'\sin\theta\cos t}\,d\varphi'\widehat{y}\\ &= C_1\frac{e^{jkr}}{4\pi r}e^{-jl\varphi}\int_0^R E(\rho')\rho'\,d\rho'\int_0^{2\pi} e^{jk\rho'\sin\theta\cos t - lt}\,d\varphi'\widehat{y}\\ &= 2\pi j^n C_1\frac{e^{jkr}}{4\pi r}e^{-jl\varphi}\int_0^R E(\rho')J_l(k\rho'\sin\theta)\rho'\,d\rho'\widehat{y}.\end{aligned} \tag{A2}$$

As mentioned in Sec. II, it is assumed that $E(\rho')$ is a constant and we ignore the effect of $2\pi j^n C_1$. According to the following integral equations [41],

$$\begin{aligned}&\int_0^1 xJ_0(ax)\,dx = \frac{J_1(a)}{a}\\ &\int_0^1 x^\mu J_\nu(ax)\,dx = a^{-\mu-1}\left[(\mu+\nu-1)\nu J_\nu(a)S_{\mu-1,\nu-1}(a) - aJ_{\nu-1}(a)S_{\mu,\nu}(a) + 2^\mu\frac{\Gamma(\frac{1}{2}+\frac{\nu}{2}+\frac{\mu}{2})}{\Gamma(\frac{l}{2}+\frac{\nu}{2}-\frac{\mu}{2})}\right],\end{aligned} \tag{A3}$$

where $S_{\mu v}()$ is the Lommel function and $\Gamma()$ is the gamma function. Then, substituting Eq. (A3) into Eq. (A2), the integral in Eq. (A4) can be rewritten as

$$\overrightarrow{\mathbf{E}}_{\text{rad}}(\mathbf{r}) = \begin{cases}\dfrac{e^{jkr}}{4\pi r}e^{-jl\varphi}R^2\dfrac{J_1(kR\sin\theta)}{kR\sin\theta}\widehat{y} & l\neq 0\\ \dfrac{e^{jkr}}{4\pi r}e^{-jl\varphi}R^2a^{-2}\left[alJ_l(a)S_{0,l-1}(a) - aJ_{l-1}(a)S_{1,l}(a) + 2\dfrac{\Gamma(1+\frac{l}{2})}{\Gamma(\frac{l}{2})}\right]\widehat{y} & l=0\end{cases} \tag{A4}$$

Considering that the analytical formula in Eq. (A4) is too complicated to be calculated, the normalized directional function can be deduced by means of Eq. (2).

APPENDIX B

The point-spread function can be expanded into the integral of a plane spectrum, as follows:

$$\frac{e^{jkr}}{2\pi r} = \frac{j}{4\pi^2}\iint_\infty \frac{e^{j(k_x x + k_y y + k_z z)}}{k_z}\,dk_x\,dk_y. \tag{B1}$$

Here, we consider a propagation case; the evanescent waves are truncated and Eq. (B1) can be approximated as follows:

$$\frac{e^{jkr}}{2\pi r} = \frac{j}{4\pi^2}\iint_{k_x^2+k_x^2\le k^2} \frac{e^{j(k_x x + k_y y + k_z z)}}{k_z}\,dk_x\,dk_y. \tag{B2}$$

According to the integral relationship of the lth Bessel function, the integral in Eq. (3) can be rewritten as follows:

$$\begin{aligned}&\int_0^R \rho' J_l\left(k\rho'\sin\theta\right)e^{-jl\varphi}\,d\rho'\\ &\quad= \frac{j^{-n}}{2\pi}\int_0^R\int_0^{2\pi}\rho' e^{j(k\rho'\sin\theta\cos\varphi' - l\varphi')}e^{-jl\varphi}\,d\varphi'\,d\rho'.\end{aligned} \tag{B3}$$

Then, using the variable substitution $\zeta = \varphi' + \varphi$ and

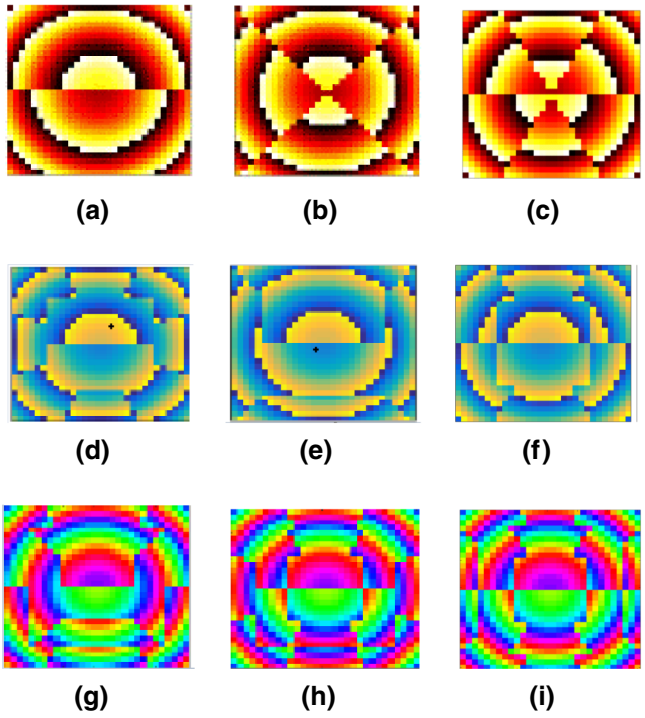

FIG. 8. The required phase-shift distributions along the metasurface: (a) $l = \pm 1$; (b) $l = \pm 2$; (c) $l = \pm 3$; (d) $l = \pm 1, l = \pm 4$; (e) $l = \pm 1, l = \pm 2$; (f) $l = \pm 1, l = \pm 3$; (g) $l = \pm 1, l = \pm 2, l = \pm 3$; (h) $l = \pm 1, l = \pm 3, l = \pm 4$; (i) $l = \pm 1, l = \pm 3, l = \pm 5$.

Substituting Eqs. (B2) and (B3) into Eq. (3), Eq. (3) can be expanded into a superposition of infinite plane waves, as shown in Eq. (5).

APPENDIX C

Some typical phase-shift distributions along the metasurface are shown in Fig. 8, based on Eqs. (10) and (12).

[1] L. Chen, J. Lei, and J. Romero, Quantum digital spiral imaging, Light Sci. Appl. **3**, e153 (2014).
[2] A. Lehmuskero, Y. Li, P. Johansson, and M. Käll, Plasmonic particles set into fast orbital motion by an optical vortex beam, Opt. Express **22**, 4349 (2014).
[3] M. Li, S. Yan, B. Yao, Y. Liang, M. Lei, and Y. Yang, Optically induced rotation of Rayleigh particles by vortex beams with different states of polarization, Phys. Lett. A **380**, 311 (2016).
[4] B. Thidé, H. Then, J. Sjöholm, K. Palmer, and J. Bergman, Utilization of Photon Orbital Angular Momentum in the Low-Frequency Radio Domain, Phys. Rev. Lett. **99**, 087701 (2007).
[5] S. Yu, L. Li, G. Shi, C. Zhu, X. Zhou, and Y. Shi, Generating multiple orbital angular momentum vortex beams using a metasurface in radio frequency domain, Appl. Phys. Lett. **108**, 121903 (2016).
[6] L. Ma, C. Chen, L. Zhou, S. Jiang, and H. Zhang, Single-layer transmissive metasurface for generating OAM vortex wave with homogeneous radiation based on the principle of Fabry-Perot cavity, Appl. Phys. Lett. **114**, 081603 (2019).
[7] M. Chen, L. Jiang, and W. Sha, Generation of orbital angular momentum by a point defect in photonic crystals, Phys. Rev. A **10**, 014034 (2018).
[8] F. Tamburini, E. Mari, A. Sponselli, B. Thidé, A. Bianchini, and F. Romanato, Encoding many channels on the same frequency through radio vorticity: First experiment test, New J. Phys. **14**, 033001 (2012).
[9] Y. Pan, S. Zhang, J. Zheng, Y. Li, X. Jin, H. Chi, and X. Zhang, Generation of orbital angular momentum radio waves based on dielectric resonator antenna, IEEE Antennas Wireless Propag. Lett. **16**, 385 (2017).
[10] J. J. Chen, Q. N. Lu, F. F. Dong, J. J. Yang, and M. Huang, Wireless OAM transmission system based on elliptical microstrip patch antenna, Opt. Express **24**, 11531 (2016).
[11] M. Barbuto, M.-A. Miri, A. Alu, F. Bilotti, and A. Toscano, Exploiting the topological robustness of composite vortices in radiation systems, Prog. Electromagn. Res. **162**, 39 (2018).
[12] H. Huang and S. Li, High-efficiency planar reflectarray with small-size for OAM generation at microwave range, IEEE Antennas Wireless Propag. Lett. **18**, 432 (2019).
[13] S. Jiang, C. Chen, H. Zhang, and W. Chen, Achromatic electromagnetic metasurface for generating a vortex wave with orbital angular momentum (OAM), Opt. Express **26**, 6466 (2018).
[14] Z. Zhang, S. Xiao, Y. Li, and B. Z. Wang, A circularly polarized multimode patch antenna for the generation of multiple orbital angular momentum modes, IEEE Antennas Wireless Propag. Lett. **16**, 521 (2017).
[15] T. Wang, R. Xie, S. Zhu, J. Gao, M. Xin, S. An, B. Zheng, H. Li, Y. Lin, H. Zhang, G. Zhai, and J. Ding, Dual-band high efficiency terahertz meta-devices based on reflective geometric metasurfaces, IEEE Access **7**, 58131 (2019).
[16] C. Li, H. Wei, and Z. Hao, Generation of electromagnetic waves with arbitrary orbital angular momentum modes, Sci. Rep. **4**, 4814 (2014).
[17] W. Zhang, S. Zheng, Y. Chen, X. Jin, H. Chi, and Xianmin Zhang, Orbital angular momentum-based communications with partial arc sampling receiving, IEEE Commun. Lett. **20**, 1381 (2016).
[18] S. Zheng, X. Hui, X. Jin, H. Chi, and X. Zhang, Transmission characteristics of a twisted radio wave based on circular traveling-wave antenna, IEEE Trans. Antennas Propag. **63**, 1530 (2015).
[19] Y. H. Cho and W. J. Byun, Generalized Friis transmission equation for orbital angular momentum radios, IEEE Trans. Antennas Propag. **67**, 2423 (2019).
[20] Y. Yao, X. Liang, M. Zhu, W. Zhu, J. Geng, and R. Jin, Analysis and experiments on reflection and refraction of orbital angular momentum waves, IEEE Trans. Antennas Propag. **67**, 2085 (2019).
[21] C. Zhang, D. Chen, and X. Jiang, RCS diversity of electromagnetic wave carrying orbital angular momentum, Sci. Rep. **7**, 15412 (2017).
[22] O. Edfors and A. J. Johansson, Is orbital angular momentum (OAM) based radio communication an unexploited area?, IEEE Trans. Antennas Propag. **60**, 1126 (2012).

[23] J. Xu, Degrees of freedom of OAM-based line-of-sight radio systems, IEEE Trans. Antennas Propag. **65**, 1996 (2017).
[24] T. Yuan, H. Wang, Y. Qin, and Y. Cheng, Electromagnetic vortex imaging using uniform concentric circular arrays, IEEE Antennas Wireless Propag. Lett. **15**, 1024 (2016).
[25] K. Liu, Y. Cheng, X. Li, Y. Qin, H. Wang, and Y. Jiang, Generation of orbital angular momentum beams for electromagnetic vortex imaging, IEEE Antennas Wireless Propag. Lett. **15**, 1873 (2016).
[26] K. Liu, Y. Cheng, Z. Yang, H. Wang, Y. Qin, and X. Li, Orbital-angular-momentum-based electromagnetic vortex imaging, IEEE Antennas Wireless Propag. Lett. **14**, 711 (2015).
[27] K. Liu, Y. Cheng, X. Li, H. Wang, Y. Qin, and Y. Jiang, Study on the theory and method of vortex-electromagnetic-wave-based radar imaging, IET Microw. Antennas Propag. **10**, 961 (2016).
[28] T. Yuan, H. Wang, Y. Qin, and Y. Cheng, Electromagnetic vortex imaging using uniform concentric circular arrays, IEEE. Antennas Wirel. Propag. Lett. **15**, 1024 (2016).
[29] S. Fürhapter, A. Jesacher, S. Bernet, and M. Ritsch-Marte, Spiral phase contrast imaging in microscopy, Opt. Express **13**, 689 (2005).
[30] L. Lin and F. Li, Beating the Rayleigh limit: Orbital-angular-momentum-based super-resolution diffraction tomography, Phys. Rev. E **88**, 033205 (2013).
[31] K. Liu, Y. Cheng, X. Li, and Y. Jiang, Passive OAM-based radar imaging with single-in-multiple-out mode, IEEE Microw. Wirel. Compon. Lett. **28**, 840 (2018).
[32] M. Lin, Y. Gao, P. Liu, and J. Liu, Super-resolution orbital angular momentum based radar targets detection, Electron. Lett. **52**, 1168 (2016).
[33] Y. Ren, Z. Wang, G. Xie, L. Li, A. J. Willner, Y. Cao, Z. Zhao, Y. Yan, N. Ahmed, N. Ashrafi, S. Ashrafi, R. Bock, M. Tur, and A. E. Willner, Atmospheric turbulence mitigation in an OAM-based MIMO free-space optical link using spatial diversity combined with MIMO equalization, Opt. Lett. **41**, 2406 (2016).
[34] G. Xie, Y. Ren, Y. Yan, H. Huang, N. Ahmed, L. Li, Z. Zhao, C. Bao, M. Tur, S. Ashrafi, and A. E. Willner, Experimental demonstration of a 200-Gbit/s free-space optical link by multiplexing Laguerre-Gaussian beams with different radial indices, Opt. Lett. **41**, 3447 (2016).
[35] Y. Yan, G. Xie, M. P. J. Lavery, H. Huang, N. Ahmed, C. Bao, Y. Ren, Y. Cao, L. Li, Z. Zhao, A. F. Molisch, M. Tur, M. J. Padgett, and A. E. Willnera, High-capacity millimetre-wave communications with orbital angular momentum multiplexing, Nat. Commun. **5**, 4876 (2014).
[36] N. Zhao, X. Li, G. Li, and J. M. Kahn, Capacity limits of spatially multiplexed free-space communication, Nat. Photonics **9**, 822 (2015).
[37] G. Gibson, J. Courtial, M. J. Padgett, M. Vasnetsov, V. Pas'ko, S. M. Barnett, and S. Franke-Arnold, Free-space information transfer using light beams carrying orbital angular momentum, Opt. Express **12**, 5448 (2004).
[38] N. Bozinovic, Y. Yue, Y. Ren, M. Tur, P. Kristensen, H. Huang, A. E. Willner, and S. Ramachandran, Terabit-scale orbital angular momentum mode division multiplexing in fibers, Science **340**, 1545 (2013).
[39] B. Jack, M. J. Padgett, and S. Franke-Arnold, Angular diffraction, New J. Phys. **10**, 103013 (2008).
[40] A. Jeffrey and H. Dai, *Handbook of Mathematical Formulas and Integrals* (Academic Press, Burlington, MA, 2008).
[41] W. Chew, *Waves and Fields in Inhomogeneous Media* (Van Nostrand Reinhold, New York, NY, 1990).